Journal of Alloys and Compounds 825 (2020) 154021

Study of the kinetics and products of the devitrification process of mechanically amorphized $Fe_{70}Zr_{30}$ alloy

A.F. Manchón-Gordón[1], J.J. Ipus[1], J.S. Blázquez[1*], C.F. Conde[1], A. Conde[1], P. Svec Sr.[2]

1 Dpto. Física de la Materia Condensada, ICMSE-CSIC, Universidad de Sevilla, P.O. Box 1065, 41080 Sevilla, Spain
2 Institute of Physics. Slovak Academy of Sciences. Dúbravská cesta 9, 845 11 Bratislava 45. Slovak Republic.
[*]The corresponding author e-mail: jsebas@us.es

ABSTRACT: Devitrification of mechanically alloyed amorphous $Fe_{70}Zr_{30}$ at. % compound consists on a two-step process: amorphous → amorphous + bcc Fe + Fe_2Zr → Fe_2Zr + $Fe_{23}Zr_6$. This sequence is inferred from the evolution of the Mössbauer spectra, the thermomagnetic experiments and the X-ray diffraction (XRD) patterns. Hyperfine parameters for both intermetallics have been obtained from Mössbauer spectroscopy in correlation with the phase identification from XRD results. The broadening of the stable compositional range of Fe_2Zr intermetallic above 1000 K is responsible for a strong dependence of the phase fractions on heating and cooling rates. Despite the overlapping of the two processes involved in the devitrification, the individual Avrami exponents of each one have been estimated.

KEYWORDS: Fe-Zr intermetallics, amorphous alloys, crystallization kinetics, nanocrystalline alloys, Mössbauer spectroscopy.

1. INTRODUCTION

Fe-Zr binary metallic glasses have received significant attention because of the stability of the phases [*Grain size stabilization of mechanically alloyed nanocrystalline Fe-Zr alloys by forming highly dispersed coherent Fe-Zr-O nanoclusters*; *In situ studies on superior thermal stability of bulk FeZr nanocomposites*] their very complex and rich

magnetic behavior, including ferromagnetism, invar and re-entrant spin-glass behavior [1-3]. Magnetic properties of these materials strongly depend on compositional changes [4, *Enhanced magnetocaloric properties of FeZr amorphous films by C ion implantation*] and on the local atomic order [5]. Therefore, the preparation method appears to be decisive to explain the different magnetic responses. The presence of two eutectic points in the Fe-Zr binary phase diagram (24 and 90 at. % Fe) [6, 7] limits rapid solidification procedures to produce completely amorphous samples only for reduced concentration ranges around the eutectic compositions. To extent these compositional ranges, other ways to produce amorphous samples are used. For example, mechanical alloying technique allows the production of amorphous samples for Fe content in the range 30-78 at. % [8]. This method has also been widely used in order to produce many other systems, such as Nb-Al [9], Cu-Cr [10] or Fe-Cu [11]. Thus these mechanically alloyed amorphous offer new homogeneous starting points to promote the crystallization of intermetallics with different compositions to that of the eutectic points.

The amorphous Fe-Zr alloys are the compositional base of the FeZr-based nanocrystalline soft magnetic materials [12], which are usually obtained after a suitable thermal treatment of the amorphous precursor. Therefore, the study of the crystallization process of the amorphous precursors have an important interest in order to control parameters such as the thermal stability of the amorphous phases against the appearing of intermetallics, the size of the crystallites or the transformed fraction. This control plays a decisive role in the magnetic properties because of the close link between the magnetic softness in nanocrystalline materials and their microstructure. In fact, crystallization of binary Fe-Zr amorphous ribbons close to the composition $Fe_{90}Zr_{10}$ has been profusely studied [13-15]. Also some studies focused on the crystallization of the Fe-Zr amorphous alloys with Fe content lower than 90 at. % can be found in the

literature [16, 17]. In the case of $Fe_{70}Zr_{30}$ at. %, amorphous system produced by milling can be found in the literature for partially amorphized samples [5], including some previous works of the authors [5, 18-20]. However, the study of the devitrification process of this system have not been reported. Apart from their interest as magnetic materials, the intermetallic phases in Fe-Zr system play an important role in the nuclear industry. In fact, Fe-Zr alloys with a high content of Zr are used as structural materials for light and heavy water based thermal reactors due to their low neutron absorption cross section and good mechanical and corrosion properties [21, 22].

In this work, with the aim of complementing a systematic study on the magnetic properties and crystallization behaviour in Fe-Zr amorphous alloys, we present a detailed study on the correlation between the magnetic behavior and structural changes taking place during the crystallization of $Fe_{70}Zr_{30}$ at. % amorphous powder produced by mechanical alloying. The products of the crystallization process have been studied by X-ray diffraction, Mössbauer spectroscopy and magnetometry. Avrami exponents of each transformation have been obtained applying the classical nucleation and growth kinetic theory extended to overlapped processes.

2. EXPERIMENTAL

An amorphous alloy with $Fe_{70}Zr_{30}$ at. % composition was prepared by high energy ball milling after 50 h at 350 rpm in a planetary ball mill Fritsch Pulverisette Vario 4. Further milling parameters and a detailed microstructural evolution of the sample with the milling time can be found elsewhere [18].

Differential thermal analysis (DTA) was carried out in a Perkin-Elmer DTA7 unit under Ar flow for both isothermal and non-isothermal experiments. Different heating rates

(β=5, 10, 20, 40 and 60 K/min) were used for non-isothermal treatments. In order to follow the progress of the transformations, heating at 10 K/min up to different temperatures (from 883 to 1223 K) was also performed. In the case of isothermal experiments, the amorphous sample was annealed 5 hours at 888 K, 10 K below the onset temperature obtained for β=10 K/min, in order to study the crystallization process from an initial value of the transformed fraction $X_{initial}^{ISO}$=0. The corresponding baselines were obtained repeating the same treatment after the complete crystallization of the sample.

Powder diffraction pattern, recorded in a Bruker D8 Advance diffractometer (Cr-Kα, λ=2.28970 Å) in a Bragg-Brentano geometry at room temperature, has been used to follow the crystallization process of the sample. Rietveld refinements were performed by TOPAS software (Version 6).

Magnetic properties were measured using a Lakeshore 7407 Vibrating Sample Magnetometer (VSM) under a constant applied magnetic field of 0.1 T. The local environment of Fe atoms was analyzed at room temperature by Mössbauer spectrometry (MS) in transmission geometry using a ^{57}Co(Rh) source. Values of the hyperfine parameters were obtained by fitting the measured spectra with the NORMOS program [23] and isomer shifts were measured relative to that of a standard foil of pure Fe at room temperature.

3. RESULTS and DISCUSSION

3.1. Characterization of Crystallization Products

Figure 1a shows the non-isothermal DTA plot taken at 10 K/min for the as-milled amorphous sample. All the features found in the curve were irreversible as they vanish in a second heating, which was used as the corresponding baseline. Two overlapped

exothermic peaks, which should correspond to two different crystallization events, can be clearly observed. No experimental deconvolution is obtained in the heating rate range from 5 to 60 K/min (see figure 1b). However, it can be observed that the fraction ascribed to the second peak decreases with the increase of the heating rate. The obtained values of effective activation energy, E_a=2.93$\pm$0.17 eV/at from both peaks (inset of Fig. 1b), were calculated by Kissinger's method [24]. This value is similar to those reported by Mishra et al. (E_a=2.72$\pm$0.10 eV/at) [5] for the same Zr containing alloy obtained by mechanical alloying.

Figure 2a shows the XRD patterns taken at room temperature of as-milled amorphous powders and those of crystalline samples after heating them at 10K/min up to the indicated temperatures to evidence the formation of the crystalline microstructure. In the as-milled powders, the characteristic peaks of bcc Fe and hcp Zr pure phases of the initial mixture disappeared completely, leading to the formation of a broad halo distinctive of the amorphous phase near 2θ=42º. Heating above 883 K leads to the emergence of several diffraction peaks superimposed to the amorphous halo and the progressive disappearance of it. The peaks appearing at lower temperatures (after heating up to 883 K) can be assigned to the Fe_2Zr crystalline phase (space group Fd-3m). In a second stage (after heating up to 993 K), peaks attributed to the $Fe_{23}Zr_6$ crystalline phase (space group Fm-3m) appear. ~~Some traces can be ascribed to zirconium oxides in the totally crystalline sample.~~ These results agree with those reported by Garitaonandia et al. [25] for the crystallization of the $Fe_{75}Zr_{25}$ at. % amorphous alloy produced by mechanical alloying. They also found that the crystallization involved the formation of the Fe_2Zr and $Fe_{23}Zr_6$ intermetallic phases as final products. However, Gorria et. al [16], for the same compound, reported that the

Fe_2Zr intermetallic is just an intermediate and not a final product in the crystallization process.

Figure 2b shows the room temperature XRD pattern corresponding to the fully crystallized sample after heated up to 1223 K at 10 K/min. Satisfactory Rietveld refinement were obtained (<GOF>=3.5, R_{wp}=4.2 %). From the fit, it can be concluded that the main crystalline phase present in the sample at room temperature is $Fe_{23}Zr_6$ with 59.2(6) wt.% and a cell parameter a=11.701(1) Å. The Fe_2Zr is clearly detected and it reaches 25.2(5) wt.% and has a cell parameter a=7.055(1) Å. Final crystal size is clearly larger for $Fe_{23}Zr_6$ phase, for which a value of 46(3) nm is achieved, meanwhile a value of 18.2(6) nm is obtained for the Fe_2Zr crystalline phase. The other 15 wt.% is divided into the ZrO and ZrO_2 phases, which are formed despite the imposed controlled atmosphere. Atomic position and the fractional coordinates of the intermetallic phases, along with the site occupancies obtained from the refinement of the diffraction pattern in the figure 2b are given in Table 1. It is worth noting that values lower than one were obtained, leading to $Fe_2Zr_{0.8}$ and $Fe_{23}Zr_{5.8}$ stoichiometries. Therefore, both intermetallics have a lower content on Zr than the theoretical one.

Figure 3 shows room temperature Mössbauer spectra of as-milled and heat treated samples up to the indicated temperatures at β=10 K/min. The spectra show the different stages of the crystallization process. A quadrupolar distribution was used to describe the paramagnetic contributions, assigned to the amorphous phase. This distribution is the unique contribution that exhibits the as-milled sample. The spectrum of the sample heated up to 883 K shows the initial stages of the crystallization, where the decrease of the contribution of the paramagnetic phase is compensated by the appearance of a hyperfine field distribution with low hyperfine fields (<B_{hf}>=7.1(1) T). Besides the quadrupolar and the hyperfine field distributions, a sextet with hyperfine field

HF=32.41(6) T appears (area fraction reaches ~6 %), which can be assigned to the formation of the α-Fe phase. The small area fraction of this contribution explains why it is not detected from XRD. In fact, it is known that MS is a more sensitive technique than XRD in order to detect small fractions of Fe phases when paramagnetic and ferromagnetic phases coexist [18].

After heating up to 973 K, the sample is totally ferromagnetic at room temperature, evidenced by the absence of any quadrupolar distribution. Four ferromagnetic sites, including the contribution of the α-Fe phase (B_{hf}=32.6(3) T), were used to fit the ferromagnetic spectra. Beyond the site corresponding to the α-Fe phase, two well defined contributions can be observed (B_{hf}=20.72(6) and 17.77(6) T). The fitted hyperfine values are in good agreement with those reported in the literature for the Fe_2Zr phase [17]. The last and wide site used at this temperature (B_{hf}=13.7(1) T) cannot be still assigned to any crystalline phase and should correspond to the remaining amorphous or interface contributions.

Above 973 K, the increase and refinement of other contributions, corresponding to the $Fe_{23}Zr_6$ phase, shows the advance of the crystallization. This can be followed from the Mössbauer spectra as a decrease of the peaks around ±6 mm/s, corresponding to the α-Fe phase, and the emergence and enhancement of peaks between 2 and 4 mm/s with the increase of the heating temperature. In fact, the sextet assigned to the α-Fe phase disappears after heating up the sample to 1073 K and new well defined sites emerge. These results are in agreement with the DTA and XRD results, showing that independent transformations simultaneously occur during the crystallization process.

The hyperfine parameters obtained from the fit of the Mössbauer spectrum at room temperature of the sample heated up to 1223 K are summarized in table 2 along with those reported in the literature for samples prepared by different methods and

compositions [17, 25]. The final fitted hyperfine values for the Fe_2Zr are in agreement with those reported in the literature for this intermetallic obtained as a solidification product from arc-melting of the same composition [17] and about 2 T higher than those reported for the crystallization of an amorphous alloy with $Fe_{75}Zr_{25}$ composition [25]. It has to be noted that the hyperfine field is strongly dependent on the Fe content [17].

The ideal site occupancy of Fe atoms in the $Fe_{23}Zr_6$ phase suggests the existence of four subspectra with different hyperfine fields with an intensity ratio 32:32:24:4, as has been reported in [25]. However, the strong overlapping between the different ferromagnetic sites, with a very similar number of Fe atoms as near neighbors (8, 8, 10 and 9 for Fe1, Fe2, Fe3, Fe4, respectively), makes very difficult to distinguish such number of subspectra. In fact, if our results for this phase are considered just as the mean values of both Fe1 and Fe2, and Fe3 and Fe4 sites, respectively, they are in good agreement with those reported in [25].

Fe_2Zr phase has two different magnetic sites with 3:1 population ratio when it is in the magnetic state. However, results in table 2 do not show the expected ratio between both contributions. The higher linewidth of the site 2 of this phase could explain this fact, suggesting that overlapping between different ferromagnetic sites corresponding to both intermetallic phases jeopardizes the quantitative agreement. In fact, when the ideal 3:1 population ratio is considered, an estimation of the contribution of each intermetallic can be done, resulting ~35 and 65 wt. % for Fe_2Zr and $Fe_{23}Zr_6$, respectively. These results are in good agreement with those obtained by Rietveld refinement when the contributions of the oxides are not considered.

Figure 4 shows the temperature dependence of the magnetization $M(T)$ at 0.1 T of the as-milled amorphous alloy on two consecutive heating-cooling cycles from room temperature up to 1200 K. On the first heating (red hollow symbols), the magnetization

remains with almost zero values up to around 600 K, indicating the paramagnetic behavior of the amorphous sample above room temperature, in agreement with the results reported for this composition [19]. Above this temperature, a slow increase of the magnetization is observed, followed by a large change in the magnetization slope around 800 K ~~(in agreement with the first DTA exotherm)~~, suggesting the formation and the progressive growth of a ferromagnetic phase with a Curie temperature higher than the measurement temperature. It is worth noting that the heating rate in the case of the VSM experiment, β~1.5 K/min, is lower than those used in DTA and showed in Figure 1. The increase of the magnetization (and the beginning of the crystallization process) at lower temperatures that those observed in Fig. 1 is expected for thermally activated process. The magnetization curve displays a maximum for T~930 K and a quick decrease at higher temperatures, reaching almost zero values above 1043 K, associated which the ferro-paramagnetic transition of the α-Fe phase at this temperature. On cooling down from 1200 K (β~1.5 K/min), the $M(T)$ curve exhibits nearly zero values down to 1000 K, where an increase occurs, suggesting the existence of a magnetic transition around this temperature. The shape of the curve is not a single Curie transition, but compositional changes of the Fe_2Zr strongly affect its magnetic behavior at this temperature range (see inset of Fig. 4). A new transition at ~480 K can be clearly observed, which could be assigned to the $Fe_{23}Zr_6$ phase. These results agree with the Mössbauer spectra, suggesting the existence of two different ferromagnetic phases at room temperature and the existence of the α-Fe phase as an intermediate and not final product. Second heating-cooling cycle gives rise to a reversible behavior up to ~800 K of the magnetization curves. However, above this temperature, heating curves show a phase arrangement due to the compositional range broadening of the Fe_2Zr phase (see inset Fig. 4). The magnetization changes are coherent with an enhancement

of Fe content in this intermetallic phase (and an enhancement in its magnetic response [17]). However, during the second cooling (at ~1.5 K/min) the system tends to a more stable situation and only two Curie transitions at 483 and 970 K appear, corresponding to $Fe_{23}Zr_6$ and Fe_2Zr phases, respectively, which are the phases detected at room temperature.

~~It is well-known that~~ Intermetallics phases in the Fe-Zr system are ferromagnetic above room temperature [26]. However, the broad stable compositional range that the Fe_2Zr phase exhibits at high temperature (see inset of Fig. 4) [27] is the responsible of discrepancies of the magnetic properties reported in the literature ~~for this intermetallic~~. In this sense, Mattern et al. [17] reported a variation of the Curie temperature of non-stoichiometric Fe_2Zr from 629 to 821 K for 67 to 79 at.% Fe, respectively, for samples produced by arc-melting. Fe-Zr phase diagram [26] shows that compositional range of Fe_2Zr becomes thinner when the temperature is lowered. This fact could explain the behavior of the magnetization curves showed in figure 4 at high temperatures (>800 K), when a broader compositional range is admitted. After a second heating cooling cycle, magnetization curves become smoother and the magnetic transition of the ferromagnetic Fe_2Zr phase into the paramagnetic state occurs at ~970 K. The second magnetic transition, assigned to the $Fe_{23}Zr_6$, occurs at 483 K. It is worth noting the increase of the phase fraction of the $Fe_{23}Zr_6$ phase after the second heating. This fact can be correlated with the DTA results, showing the increase of the phase fraction of $Fe_{23}Zr_6$ intermetallic with the timelength of the sample at high temperatures, i.e. as heating rate decreases.

3.2. Crystallization Kinetics

Figure 5a shows the experimental Avrami exponent as a function of the transformed fraction in isothermal and non-isothermal regimes. In the first case, the transformed

fraction was obtained as $X = \Delta H_{iso}(t)/\Delta H_{total}^{iso}$, where $\Delta H_{iso}(t)$ is the enthalpy at a time t and is obtained from integrating the isothermal DTA peak up to this time, and ΔH_{total}^{iso} is the total enthalpy of the crystallization process. The Avrami exponent is then calculated, from JMAK equation, as:

$$n = \frac{d(\ln[-\ln(1-X)])}{d(\ln(t-t_0))} \quad (1)$$

For non-isothermal regime, the transformed fraction was approximated to the normalized transformed enthalpy, $X = \Delta H(T)/\Delta H_{total}^{non-iso}$, where $\Delta H(T)$ is the enthalpy developed up to temperature T and $\Delta H_{total}^{non-iso}$ is the total enthalpy of the crystallization process. In this case, Avrami exponent was studied using a direct approach to non-isothermal processes of the JMAK theory [28] as:

$$\frac{d(\ln[-\ln(1-X)])}{d(\ln[\frac{T-T_0}{\beta}])} = n\left\{1 + \frac{E_a}{RT}(1 - \frac{T_0}{T})\right\} \quad (2)$$

where E_a is the activation energy, R the universal gas constant and T_0=$T_p/2$, being T_p the peak temperature, is an effective onset temperature that minimizes the error of the approximation performed [29]. As can be observed in the figure, the values obtained in the isothermal case are close to the unity along the transformation, typical of nanocrystallization processes for which growth is severely impinged [30]. In fact, Rietveld fit of the XRD spectra after isothermal treatment (Fig. 5b) leads to a crystal size of 13.3(10) and 39(7) nm for Fe_2Zr and $Fe_{23}Zr_6$ phases, respectively, lower than those obtained in the case of non-isothermal regime. It is also worth mentioning that in this case, the majority phase is the Fe_2Zr (almost 50%), in contrast with the non-isothermal regime. This is in agreement with the DTA curves, confirming the high dependence of $Fe_{23}Zr_6$ phase fraction with the heat treatment and with the crystallization sequence concluded from XRD and Mössbauer spectrometry. It has been determined

that Fe_2Zr intermetallic is formed during the first exothermic peak whereas $Fe_{23}Zr_6$ phase is a product of the second transformation process.

In the case of the non-isothermal regime, a bimodal behavior of the Avrami exponent can be observed, in agreement with the DTA and XRD results, that shows two overlapped transformations during the crystallization process (formation of the Fe_2Zr and $Fe_{23}Zr_6$ crystalline phases). In order to obtain the JMAK parameters of the individual transformations, a procedure previously proposed for two amorphous $Fe_{90}Zr_{10}$ and $(Fe_{0.7}Co_{0.3})_{90}Zr_{10}$ melt-spun ribbons [31] was applied. Following it, the local Avrami exponents obtained for transformations implying multiple processes can lead to the actual parameters of the individual processes as:

$$n_N = n^* - \frac{dn^*}{dX}(1-X)ln(1-X) \quad (3)$$

where n^* is the value of the experimental effective local Avrami exponent of the complete transformation (showed in Fig. 5a) and n_N is the Avrami exponent of the last process. On the other hand, it is possible to obtain the corresponding fraction of the last process f_N as:

$$\ln(f_N) = -\frac{1}{n_N}(1-X)[\ln(1-X)]^2\frac{dn^*}{dX} \quad (3)$$

Figure 6a shows $\mathrm{d}X/\mathrm{d}T$ vs X for a sample heated at 10 K/min where the vertical lines mark the corresponding X range (X=0.63-0.72) for which nearly constant values of n_2=2.0$\pm$0.2 (see Fig. 6b) and f_2=0.47$\pm$0.03 (see Fig. 6c) were obtained. Once the final fraction of each process is known, it is possible to directly obtain the local values of the individual processes in the regions not affected by the overlapping. This is shown in figure 7 along with the effective local Avrami exponent n^* for comparison. The average value of the Avrami exponents for the crystallization of the Fe_2Zr phase is $<n_1>$=1.42$\pm$0.05. It should indicate the presence of quenched nuclei in the alloy and

three dimensional growth controlled by diffusion. Similar results are obtained in the case of the crystallization of the $Fe_{23}Zr_6$ phase, with values obtained starting from ~1.5, but only for *X* below ~0.8 and rapidly decreasing, even below ~1. Although these deviations are typically found and generally ascribed to baseline determination artifacts, this result is in qualitative agreement with the theoretical predictions of the multiple process interpretation of the nanocrystallization [30]. Moreover, it is also worth noting that a decreasing of the activation energy along the crystallization could imply an underestimation of the Avrami exponents [28].

~~On the other hand,~~ The differences between isothermal and non-isothermal kinetic results for the individual processes could be ascribed to a stronger impingement in the growth of the intermetallic phases in isothermal regime (lower temperatures imply slower diffusivities), in agreement with the XRD results, that show smaller crystallite size for the isothermal treatment.

4. CONCLUSIONS

The crystallization products and crystallization kinetics of amorphous $Fe_{70}Zr_{30}$ at. % alloy prepared by high energy ball milling have been studied. The combination of X-ray diffraction, Mössbauer spectroscopy and thermomagnetic experiments shows that the crystallization takes place in a two-overlapped processes. During the first step, Fe_2Zr and α-Fe phase coexist with a remaining amorphous matrix. The second step involves the formation of the $Fe_{23}Zr_6$ crystalline phase along as the remaining amorphous matrix and the α-Fe phase disappear. The results obtained from the different techniques agree between them and allow us a clear assignment of microstructural and hyperfine parameters at room temperature as well as the Curie temperatures to each intermetallic phases. The broadening of the compositional range of Fe_2Zr phase at high temperatures

explains the evolution of the magnetization curves and the high dependence of the phases fraction on thermal treatments.

JMAK theory has been used to describe the crystallization process in both isothermal and non-isothermal regimes. In the case of the non-isothermal regime, the local Avrami exponent of the independent transformations have been obtained using a procedure to describe simultaneous processes leading to the formation of different phases. A stronger growth impingement in the isothermal regime can explain the lower Avrami exponent found with respect to those obtained for non-isothermal treatments.

Acknowledgements

This work was supported by AEI/FEDER-UE (Project MAT 2016-77265-R) and the PAI of the Regional Government of Andalucía. Support of the project APVV-15-0621 is also acknowledged. A.F. Manchón-Gordón acknowledges his contract to the VPPI-US of the University of Sevilla.

References

[1] Unruh KM, Chien CL. MAGNETIC-PROPERTIES AND HYPERFINE INTERACTIONS IN AMORPHOUS FE-ZR ALLOYS. Physical Review B 1984;30:4968-74.
[2] Kaul SN, Siruguri V, Chandra G. MAGNETIZATION AND MOSSBAUER STUDY OF THE REENTRANT AMORPHOUS FE90ZR10 ALLOY. Physical Review B 1992;45:12343-56.
[3] Barandiaran JM, Gorria P, Orue I, FdezGubieda ML, Plazaola F. Tensile stress dependence of the Curie temperature and hyperfine held in Fe-Zr-B-(Cu) amorphous alloys. Physical Review B 1996;54:3026-9.
[4] Altounian Z, Stromolsen JO. SUPERCONDUCTIVITY AND SPIN FLUCTUATIONS IN CU-ZR,NI-ZR,CO-ZR AND FE-ZR METALLIC GLASSES. Physical Review B 1983;27:4149-56.
[5] Mishra D, Perumal A, Srinivasan A. Magnetic properties of mechanically alloyed Fe(100-x)Zr(x) (20 <= x <= 35) powder. Journal of Physics D-Applied Physics 2008;41.
[6] Malakhova TO, Alekseyeva ZM. THE ZR-FE PHASE-DIAGRAM IN THE RANGE 20 - 40 AT-PERCENT FE AND THE CRYSTALLINE-STRUCTURE OF THE INTERMETALLIC COMPOUND ZR3FE. Journal of the Less-Common Metals 1981;81:293-300.
[7] Granovsky MS, Arias D. Intermetallic phases in the iron-rich region of the Zr-Fe phase diagram. Journal of Nuclear Materials 1996;229:29-35.
[8] Schultz L. FORMATION OF AMORPHOUS METALS BY MECHANICAL ALLOYING. Materials Science and Engineering 1988;97:15-23.
[9] Li XH, Wen X, Zhao HH, Ma ZQ, Yu LM, Li C, et al. The formation and evolution mechanism of amorphous layer surrounding Nb nano-grains in Nb-Al system during mechanical alloying process. Journal of Alloys and Compounds 2019;779:175-82.
[10] Aguilar C, Martinez VD, Palacios JM, Ordonez S, Pavez O. A thermodynamic approach to energy storage on mechanical alloying of the Cu-Cr system. Scripta Materialia 2007;57:213-6.
[11] Jiang JZ, Gente C, Bormann R. Mechanical alloying in the Fe-Cu system. Materials Science and Engineering a-Structural Materials Properties Microstructure and Processing 1998;242:268-77.
[12] McHenry ME, Willard MA, Laughlin DE. Amorphous and nanocrystalline materials for applications as soft magnets. Progress in Materials Science 1999;44:291-433.
[13] Zarubova N, Moser N, Kronmuller H. KINETICS OF CRYSTALLIZATION IN A FE90ZR10 AMORPHOUS ALLOY. Materials Science and Engineering a-Structural Materials Properties Microstructure and Processing 1992;151:205-15.
[14] Abrosimova GE, Aronin AS. Phase segregation in the Fe90Zr10 amorphous alloy under heating. Physics of the Solid State 1998;40:1603-6.
[15] Liu XD, Liu XB, Altounian Z. Structural evolution of Fe33Zr67 and Fe90Zr10 metallic glasses. Journal of Non-Crystalline Solids 2005;351:604-11.
[16] Gorria P, Garitaonandia JS, Perez MJ, Blanco JA, Campo J. Crystallization of Fe75Zr25 metallic glass: a two-step process involving metastable bcc-Fe and polymorphic transformation. Physica Status Solidi-Rapid Research Letters 2009;3:28-30.
[17] Mattern N, Zhang WX, Roth S, Reuther H, Baehtz C, Richter M. Structural and magnetic properties of non-stoichiometric Fe2Zr. Journal of Physics-Condensed Matter 2007;19.
[18] Manchón-Gordón AF, Ipus JJ, Blázquez JS, Conde CF, Conde A. Evolution of Fe environments and phase composition during mechanical amorphization of Fe70Zr30 and Fe70Nb30 alloys. Journal of Non-Crystalline Solids 2018;494:78-85.
[19] Manchón-Gordón AF, Ipus JJ, Moreno-Ramírez LM, Blázquez JS, Conde CF, Franco V, et al. Correction of the shape effect on magnetic entropy change in ball milled Fe70Zr30 alloys. Journal of Alloys and Compounds 2018.
[20] Blazquez JS, Franco V, Conde A. Enhancement of the magnetic refrigerant capacity in partially amorphous Fe70Zr30 powders obtained by mechanical alloying. Intermetallics 2012;26:52-6.

[21] Zander D, Koster U. Corrosion of amorphous and nanocrystalline Zr-based alloys. Materials Science and Engineering a-Structural Materials Properties Microstructure and Processing 2004;375:53-9.
[22] Botta WJ, Berger JE, Kiminami CS, Roche V, Nogueira RP, Bolfarini C. Corrosion resistance of Fe-based amorphous alloys. Journal of Alloys and Compounds 2014;586:S105-S10.
[23] Brand RA, Lauer J, Herlach DM. THE EVALUATION OF HYPERFINE FIELD DISTRIBUTIONS IN OVERLAPPING AND ASYMMETRIC MOSSBAUER-SPECTRA: A STUDY OF THE AMORPHOUS ALLOY PD77.5-XCU6SI16.5FEX. Journal of Physics F-Metal Physics 1983;13:675-83.
[24] Kissinger HE. REACTION KINETICS IN DIFFERENTIAL THERMAL ANALYSIS. Analytical Chemistry 1957;29:1702-6.
[25] Garitaonandia JS, Suzuki K, Cashion JD, Goikolea E, Insausti M, Plazaola F, et al. Mossbauer study of the crystallization products of a Fe75Zr25 amorphous alloy. Hyperfine Interactions 2005;165:161-5.
[26] Massalski TBe. Binary Alloy Phase Diagrams ASM International. Ohio1996.
[27] Jiang M, Oikawa K, Ikeshoji T, Wulff L, Ishida K. Thermodynamic calculations of Fe-Zr and Fe-Zr-C systems. Journal of Phase Equilibria 2001;22:406-17.
[28] Blazquez JS, Conde CF, Conde A. Non-isothermal approach to isokinetic crystallization processes: Application to the nanocrystallization of HITPERM alloys. Acta Materialia 2005;53:2305-11.
[29] Blazquez JS, Borrego JM, Conde CF, Conde A, Lozano-Perez S. Extension of the classical theory of crystallization to non-isothermal regimes: Application to nanocrystallization processes. Journal of Alloys and Compounds 2012;544:73-81.
[30] Manchon-Gordon AF, Blazquez JS, Conde CF, Conde A. Nanocrystallization kinetics understood as multiple microprocesses following the classical theory of crystallization. Journal of Alloys and Compounds 2016;675:81-5.
[31] Blazquez JS, Conde CF, Conde A. On the use of classical JMAK crystallization kinetic theory to describe simultaneous processes leading to the formation of different phases in metals. International Journal of Thermal Sciences 2015;88:1-6.

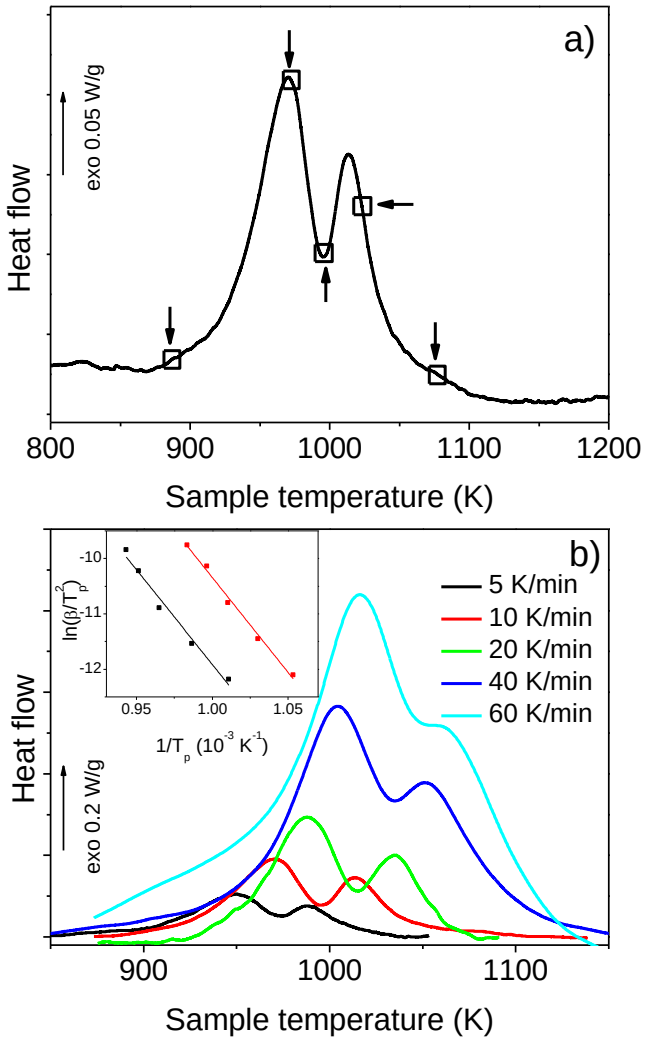

Figure 1. a) Non-isothermal DTA scan at 10 K/min for the as-milled sample. Arrows indicate the corresponding temperatures up to which different samples have been heated. b) Non-isothermal DTA scans for as-milled samples at different heating rates in the region of the DTA exotherm. The inset shows the Kissinger's plots for both peaks.

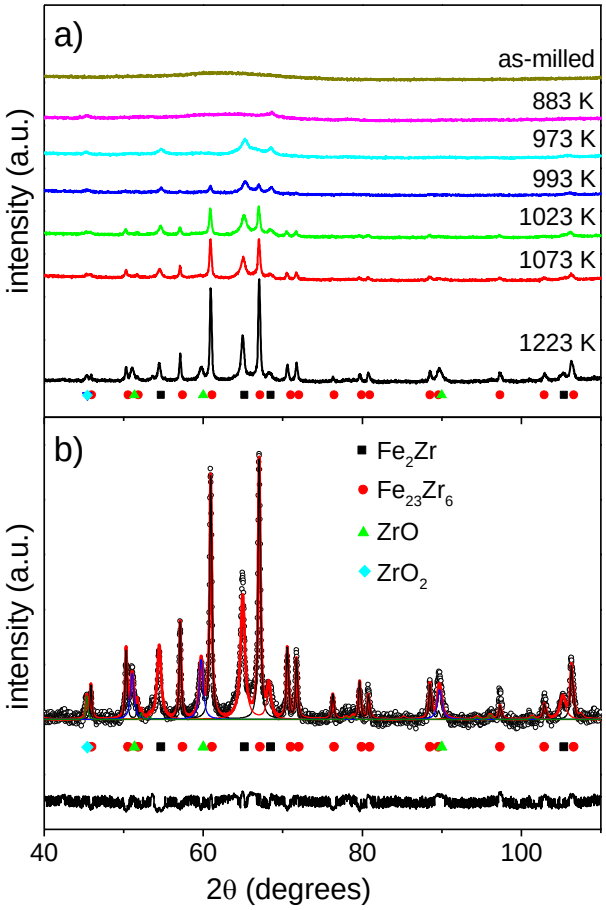

Figure 2. a) XRD patterns taken at room temperature of as-milled amorphous powders and of samples heated at 10 K/min up to the indicated temperatures. These temperatures correspond to those marked by arrows in Figure 1a. b) Experimental (points) and Rietveld calculated (lines) patterns from room temperature XRD of the fully crystallized sample heated up to 1223 K at 10K/min. Symbols correspond to the position of the Bragg reflections. The observed-calculated difference is shown at the bottom of the figure.

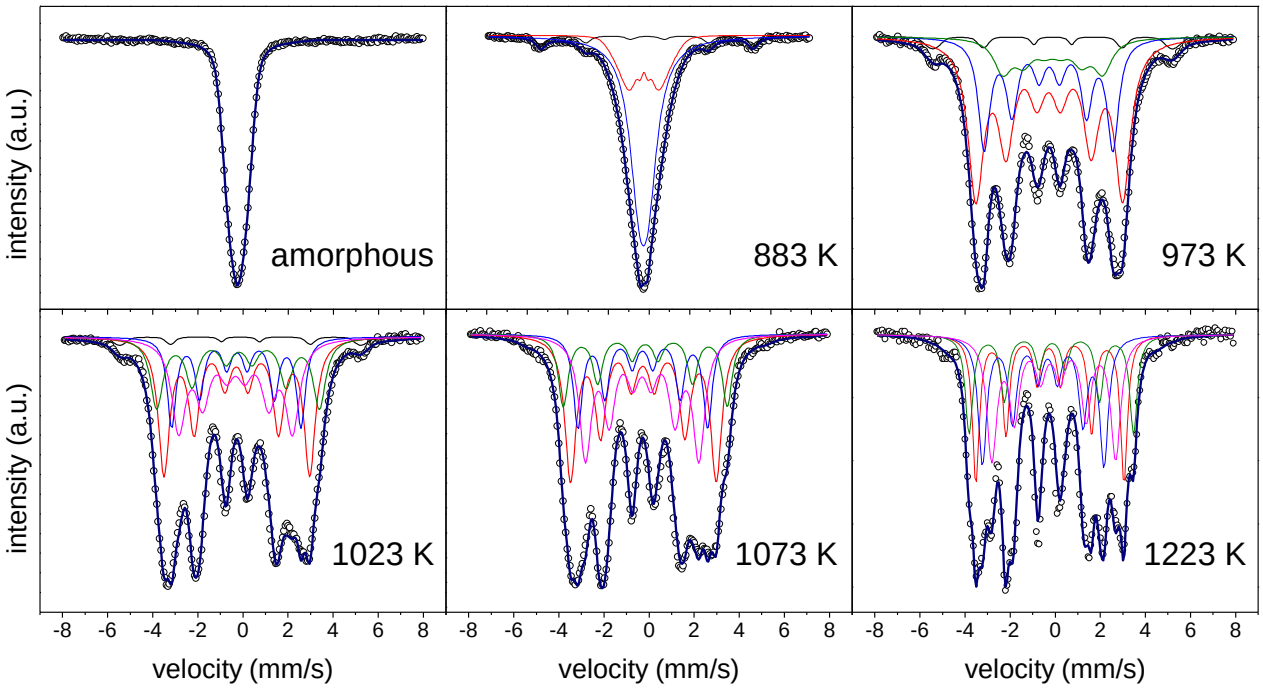

Figure 3. Experimental room temperature Mössbauer spectra (symbols) and model fitting (lines) of as-milled sample and of heat treated samples up to the indicated temperatures. These temperatures correspond to those marked by arrows in Figure 1a

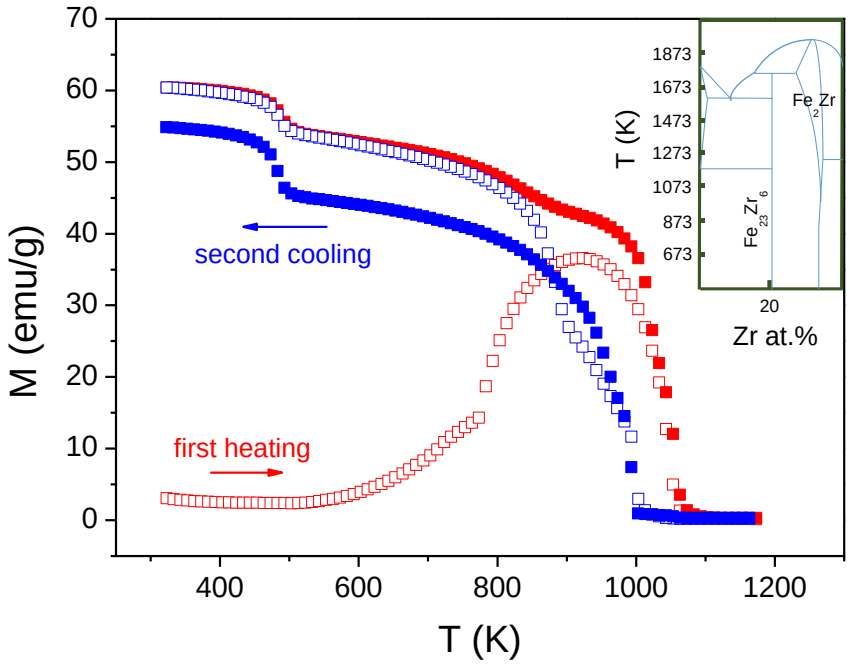

Figure 4. Magnetization versus temperature curves under a constant magnetic field of 0.1 T, on a first heating (red hollow symbols)-cooling (blue hollow symbols) cycle up to 1200 K and a second heating-cooling cycle (filled symbols). Inset: Schematic diagram of Fe-Zr system adapted from [27].

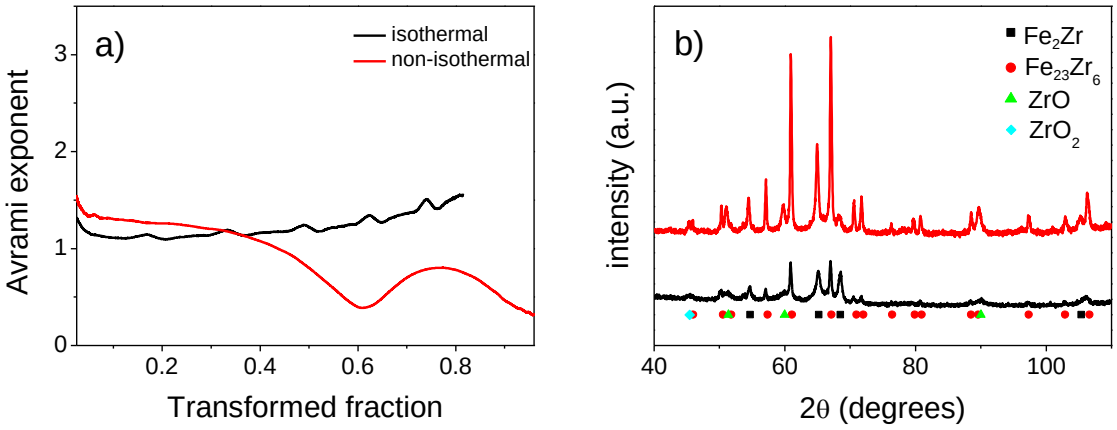

Figure 5. a) Experimental local Avrami exponents as a function of transformed fraction of the crystallization process for $Fe_{70}Zr_{30}$ at. % amorphous alloy for isothermal (5 h at 888 K) and non-isothermal (10 K/min up to T=1223 K) treatments. b) XRD patterns at room temperature of samples submitted to each treatment.

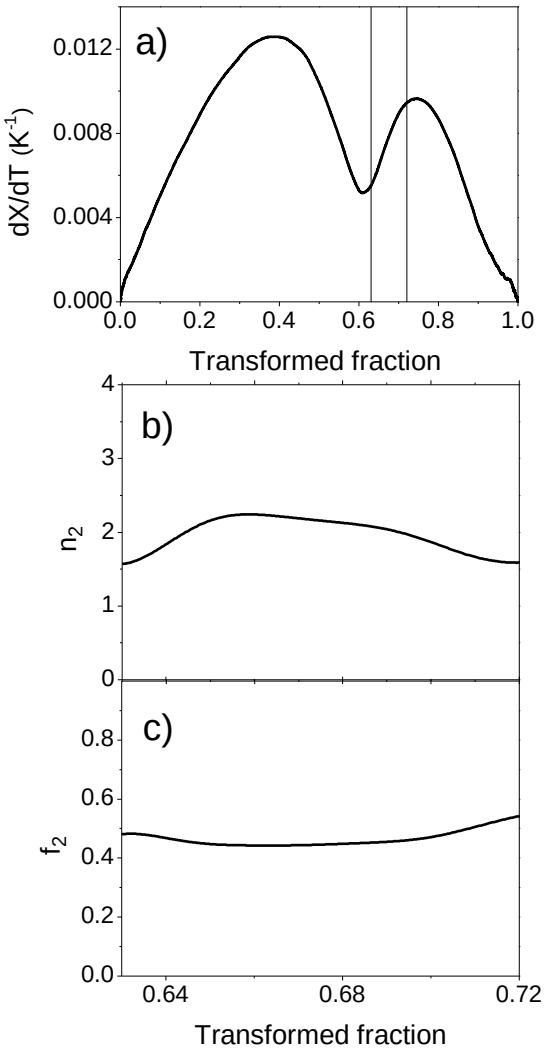

Figure 6. a) Rate of change of the transformed fraction with temperature as a function of the transformed fraction. Vertical lines indicate the range shown in the lower panels. b) Avrami exponent of the final process calculated from Eq. 3. c) Maximum transformed fraction corresponding to the final process calculated from Eq. 4. All the panels correspond to the crystallization process at β=10 K/min.

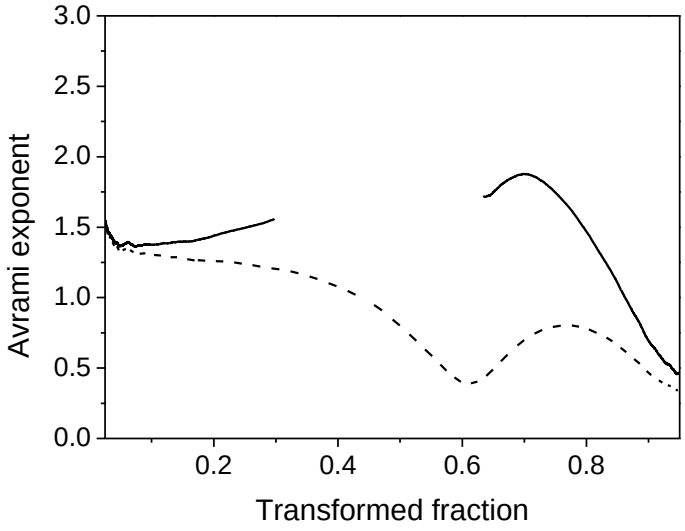

Figure 7. Calculated Avrami exponents for the first and second processes (solid lines) as a function of the total transformed fraction. Values of the effective Avrami exponent for the complete process (dotted lines) are also shown.

	Atom	Wyckoff position	x	y	z	occupation
Fe_2Zr	Fe1	16d	0.625	0.625	0.625	1
	Zr1	8a	0	0	0	0.80(1)
$Fe_{23}Zr_6$	Fe1	4b	0.5	0.5	0.5	0.85(3)
	Fe2	24d	0	0.25	0.25	0.87(1)
	Fe3	32f	0.378	0.378	0.378	0.88(1)
	Fe4	32f	0.178	0.178	0.178	0.98(1)
	Zr1	24e	0.203	0	0	0.85(1)

Table 1. Fractional atomic coordinates and occupancies for Fe_2Zr and $Fe_{23}Zr_6$ obtained after Rietveld refinement to the XRD pattern taken at room temperature of the sample heated up to 1223 K at 10 K/min.

Technique	Component		B_{hf} (T)	δ (mm/s)	Q (mm/s)	A (%)	λ (mm/s)	Ref.
Mechanical alloying ($Fe_{70}Zr_{30}$) + heating treatment	Fe_2Zr	site1	20.35(3)	-0.159(3)	0.06(2)	25	0.37(1)	This work
		site2	17.02(4)	-0.049(3)	0.02(2)	30	0.54(1)	
	$Fe_{23}Zr_6$	site1	16.70(2)	-0.329(4)	0.01(1)	27	0.45(1)	
		site2	22.59(3)	-0.059(3)	0.02(2)	18	0.40(1)	
Mechanical alloying ($Fe_{75}Zr_{25}$) + heating treatment	Fe_2Zr	site1	18.3(1)	-0.18(2)	-0.03(2)		0.46(4)	[25]
		site2	16.5(1)	-0.19(2)	-0.04(3)		0.46(4)	
	α-Fe	site1	33.0(1)	0.00(1)	0.00(1)		0.31(2)	
		site2	30.5(2)	0.03(3)	-0.1(1)		0.63(2)	
	$Fe_{23}Zr_6$	site1	16.0(1)	-0.18(1)	0.03(1)		0.47(3)	
		site2	16.6(2)	-0.19(2)	-0.01(1)		0.47(3)	
		site3	23.8(1)	-0.04(1)	-0.01(1)		0.47(3)	
		site4	21.5(2)	-0.13(1)	0.02(2)		0.47(3)	
Arc melting ($Fe_{70}Zr_{30}$) + heating treatment	Fe_2Zr	site1	20.6	-0.193	0.114	75	0.470	[17]
		site2	18.8	-0.190	-0.174	25	0.470	

Table 2. Hyperfine parameters at room temperature of sample heated up to 1223 K at 10 K/min along with those of other FeZr alloys from the literature. B_{hf} is the magnetic hyperfine field, δ the isomer shift relative to α-Fe, Q the quadrupole splitting, A is the relative contribution of the component and λ is the linewidth of each contribution.